Arvind Jaikumar
Microsystems Engineering Department,
Rochester Institute of Technology,
76 Lomb Memorial Drive,
Rochester, NY 14623
e-mail: aj4853@rit.edu

Aniket Rishi
Mechanical Engineering Department,
Rochester Institute of Technology,
76 Lomb Memorial Drive,
Rochester, NY 14623
e-mail: amr6756@rit.edu

Anju Gupta
Chemical Engineering Department,
Rochester Institute of Technology,
76 Lomb Memorial Drive,
Rochester, NY 14623
e-mail: argche@rit.edu

Satish G. Kandlikar[1]
Fellow ASME
Mechanical Engineering Department,
Rochester Institute of Technology,
76 Lomb Memorial Drive,
Rochester, NY 14623;
Microsystems Engineering Department,
Rochester Institute of Technology,
Rochester, NY 14623
e-mail: sgkeme@rit.edu

Microscale Morphology Effects of Copper–Graphene Oxide Coatings on Pool Boiling Characteristics

Enhanced pool boiling heat transfer, with simultaneous increase in critical heat flux (CHF) and heat transfer coefficient (HTC), is desired to improve overall system efficiency and reduce equipment size and cost. This paper focuses on combining graphene oxide (GO) and porous copper particles to generate microstructures based on their ability to enhance HTC, CHF, or both. Three pool boiling performance characteristics based on CHF improvements and wall superheat reductions are identified: Type I—reduction in wall superheat only, type II—increase in CHF only, and type III—increase in CHF with reduction in wall superheat at higher heat fluxes. Specific microscale morphologies were generated using (a) screen-printing and (b) electrodeposition techniques. In type-I, rapid bubble activity due to increased availability of nucleation cavities was seen to influence the reduction in the wall superheats, while no increase in CHF was noted. Roughness-augmented wettability was found to be the driving mechanism in type-II enhancement, while wicking and increased nucleation site density were responsible for the enhancement in type-III. An HTC enhancement of ~216% in type-I and a CHF improvement of ~70% in type-II were achieved when compared to a plain copper surface with water. In type-III enhancement, a CHF of 2.2 MW/m^2 (1.8× over a plain surface) with a HTC of 155 kW/m^2 °C (~2.4× over a plain surface) was obtained. Furthermore, close correlation between the boiling performance and the microscale surface morphology in these three categories has been identified. [DOI: 10.1115/1.4036695]

Introduction

The latent heat transfer enables removal of large quantities of heat through the process of boiling. It finds application in boilers, evaporators, and integrated chip cooling which makes it an active research topic. Boiling can be of two types: (i) pool boiling—where the liquid flow over the heater surface is dominated by natural convection and (ii) flow boiling—where liquid is forced over the heat exchange region using pumps. Nucleate boiling is widely recognized as an effective method to dissipate heat efficiently. Two performance parameters that are used to characterize the boiling process are the CHF and HTC. CHF is a condition that determines the upper limit of nucleate boiling and is characterized by a vapor layer blanketing the boiling surface. It leads to a dramatic increase in the surface temperature in a heat flux controlled system. The HTC determines how effectively heat is being removed from the surface to the boiling liquid under a given temperature difference. This has led to recent research efforts for developing surfaces directed toward simultaneously increasing the CHF and HTC limits.

Figure 1 provides a summary of the enhancement mechanisms available in literature and the scale of enhancement features employed by the researchers. The classification provided by Kandlikar [12] is used as a guidance in the figure. The enhancement mechanisms shown are the additional surface area, increased nucleation sites, wettability control, wicking enabled structures, microlayer-partitioning, and enhanced macroconvection using separate liquid–vapor pathways. The most conventional technique for enhancing the heat transfer performance is by increasing the heat transfer surface area. Mandrusiak and Carey [1] employed offset strip-fin geometry with heights ranging from 3.8 mm to 9.5 mm. Pastuszko and Piasecka [2] employed mini-fins with height range of 0.5–1 mm and used FC-72 as the working fluid. The highest heat transfer coefficients were reported with the 1 mm tall fin. However, in such enhancements, the effect of thermal resistance in the tall fins significantly reduces the HTC.

In a recent approach, separate liquid–vapor pathways were provided in the immediate vicinity of the heater surface to simultaneously increase the CHF and HTC. Kandlikar [12] introduced enhanced macroconvection as a new boiling mechanism which is very effective outside the influence region of a bubble. This mechanism was exploited using evaporation momentum force in a contoured-fin structure to control the bubble trajectory on the surface. Similarly, Cooke and Kandlikar [13] demonstrated that open microchannels can be used as conduits to supply the returning liquid toward the nucleation sites. Jaikumar and Kandlikar [5,6] coated sintered porous particles selectively on fin-tops, channel-walls, and throughout the open microchannel surface. Separate liquid–vapor pathways in these configurations resulted in a record CHF of 420 W/cm^2 at a wall superheat of 1.9 °C with a HTC of 2.9 MW/m^2 °C. In another arrangement, nucleating regions with a network of feeder channels resulted in a CHF of 394 W/cm^2 and an HTC of 713 kW/m^2 °C [14].

In another modification type, additional nucleation sites were generated through porous coatings [3,15]. These coatings present two advantages: (i) reduce boiling incipience by initiating nucleation through entrapped gases in the cavities and (ii) enhance thin film evaporation in the porous matrix through increased wicking. Webb [15] conducted a series of experiments to understand the geometrical parameters affecting the boiling performance. Coating thickness was identified as an important parameter and coating layers of 3–4 times the particle diameter were found to be

of optimum thickness for copper. In an extension of this understanding, Li and Peterson [3] conducted a parametric study and identified that the effect of thermal resistance and availability of additional nucleation sites need to be carefully weighed in designing these structures.

Wicking and wettability structures are attractive due to their ability to retain liquid for additional evaporation which results in enhanced CHFs. Rahman et al. [8] used bio-templated virus to generate micropillar wick structures. Through this technique, they demonstrated that the wicked volume flux determined the increase in CHF. O'Hanley et al. [16] demonstrated the separate effects of wettability, porosity, and roughness on CHF. They demonstrated that 50–60% enhancement in CHF was obtained with a hydrophilic porous surface. Betz et al. [10] showed that superhydrophilic surface with superhydrophobic islands significantly improves the CHF and HTC.

A number of publications have suggested that graphene can be used as a boiling enhancement coating [17–20]. The synthesis technique employed for graphene is seen to play an important role in the outcome. The basis of these manufacturing techniques relies on overcoming the weak Van-der-Waals forces holding the graphitic layers together. Mechanical and liquid exfoliation are the popular techniques employed to produce graphene sheets. Liquid-exfoliation is an attractive option for nanofluids-based boiling studies, since the manufacturing protocols are relatively relaxed compared to its mechanical exfoliation counterparts [21]. However, the trade-off in such techniques is the addition of oxygen molecules and functional groups (carboxyl and hydroxyl) to the basal structure of the graphene hexagonal matrix resulting in GO structures.

A comprehensive summary outlining the enhancements from boiling GO nanofluids is provided in Ref. [22]. The enhancements primarily arise from self-assembly characteristics [23], improved wettability [18], and thermal conductivity [24]. Kim et al. [25] reported that highly hydrophobic wetting was also reported as a consequence of layer build up on the substrates. Raj et al. [26] have shown that the advancing contact angles are a true representation of wettability in graphene coatings, while the receding contact angles were dictated by the defects on the surface which results in contact angle hysteresis.

Jaikumar et al. [22,27] used monolayer, multilayer, and dip-coated graphene coatings on copper substrates to explain the heat transfer enhancement mechanisms. Defects induced by coating techniques in mono and multilayer samples were shown to result in a very large contact angle hysteresis (>60 deg) in their study. For thicker coatings (in excess of six layers), such as the dip-coated surfaces, roughness and microlayer partitioning mechanisms were seen to be responsible for the enhancement. The microlayer partitioning mechanism resulted in a maximum CHF on nonwicking graphene coatings.

As seen from literature, GO coatings are shown to be nonwicking, and benefit from thermal conductivity, contact angle hysteresis, and enhanced microlayer partitioning mechanisms. In this paper, the wickability in graphene coatings is introduced by combining porous copper particle coatings and GO sheets. These wickability features will have the capability to retain the liquid film for enhanced evaporation, which results in higher CHFs and HTCs. The coatings were prepared using (i) screen-printing and (ii) electrochemical (galvanostatic and chronoamperometry) methods. This paper presents the chemical characterization of the prepared surfaces using (i) Fourier-transform infrared spectroscopy (FTIR) and (ii) scanning electron microscopy (SEM). The close relation between the observed microscale morphological features and the heat transfer results are discussed.

Concept and Hypothesis

In this work, we categorize the boiling characteristics based on the increase in CHF and decrease in wall superheats (Fig. 2). Three distinct boiling characteristics identified here are

Type-I: In this type, the surfaces exhibit a decrease in wall superheat without a significant increase in CHF. The CHFs obtained on these surfaces are similar to that on the baseline surface.

Type-II: In this type, the surfaces exhibit an increase in CHF without significant reduction in wall superheats. The wall superheats obtained on these surfaces are similar to that on the baseline surface.

Type-III: In this type, the surfaces exhibit an increase in CHF with a simultaneous decrease in wall superheats at higher heat fluxes. These types of surfaces are extremely beneficial as they offer increased operating ranges as well as efficient heat transfer.
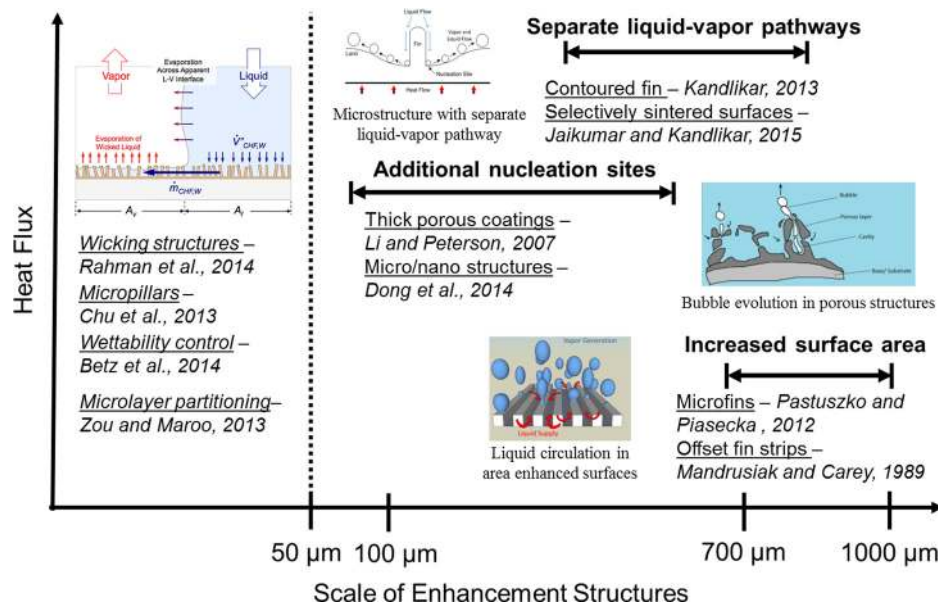

Fig. 1 Schematic representation summarizing enhancement features used in literature—increased surface area [1,2], additional nucleation sites [3,4] (reprinted with permission from Patil and Kandlikar (2014), copyright 2014 Elsevier), separate liquid–vapor pathways [5–7] (reprinted with permission from Kandlikar (2013), copyright 2013 AIP publishing LLC), wicking [8] (reprinted with permission from Rahman et al. (2014), copyright 2014 American Chemical Society), roughness [9], wettability [10], and microlayer-partitioning [11]
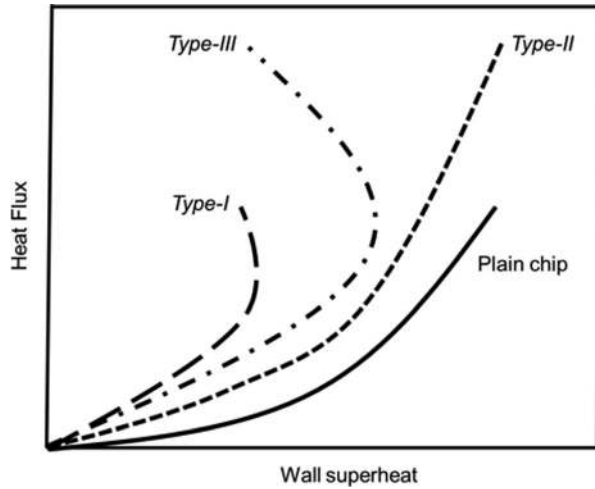
Fig. 2 Schematic representation of the three boiling characteristics identified in this study. Type-I: reduced wall superheat; type-II: increased CHF without reduction in wall superheat; and type-III: increased CHF with reduction in wall superheat at higher heat fluxes.

Controlled experiments were conducted to demonstrate the three boiling characteristics identified in Fig. 2. Increasing evaporation rates from the microlayer under a bubble has been found to increase the boiling performance as demonstrated by Kandlikar [12], Maroo [28], and Zou et al. [29]. This can be achieved by increasing the microlayer volume under a growing bubble [8,11]. Wick structures utilize the irregularly shaped matrix around curved interfaces to contain the extra volume for evaporation. These structures significantly increase the CHF by preventing dry-out condition due to liquid retention in the wick structure. On the other hand, nonwicking graphene coatings have shown to increase CHF by wettability changes and microlayer partitioning mechanisms. Therefore, the current work focuses on combining porous structures with GO coatings to demonstrate the three boiling characteristics identified through morphology-driven effects. Typical GO-based coatings are considered to be nonwicking [22]. In the GO sheets employed here, the liquid droplet volume did not change significantly over time for a copper sample coated with GO. Therefore, the GO sheets employed here were considered to be nonwicking. However, additional dynamics of the wick structure introduced by the porous copper structures is expected to significantly alter the performance characteristics and is evaluated in this paper.

Experimental Setup

An experimental setup similar to that employed by Jaikumar and Kandlikar [5] was used in this study as shown in Fig. 3. The main components of the test setup were the test section, the water bath, and the heat source. A copper test chip was held in a ceramic chip holder on the bottom garolite plate. A quartz glass (custom manufactured by: Friedrich and Dimmock Inc., Millville, NJ) water bath was assembled over the test section. A rubber gasket was used to ensure good seal between the test section and the water bath. A steel head cap screw was used to hold a water reservoir between the middle garolite plate and the top aluminum plate. The reservoir replenished water in the quartz glass bath on high rates of evaporation encountered during the boiling process. The top aluminum plate was provided with openings for the saturation thermocouple probe and a 60-VDC, 200 W cartridge heater to maintain water in the reservoir at saturation by boiling it continuously.

Heat was supplied to the test section using a copper heater block with four 120-VDC, 200 W cartridge heaters. The heater block was machined such that only the 1 cm^2 area was exposed to the water at the top of the test section, ensuring 1D conduction

which eliminated the heat spreading effect. Additionally, the copper block was housed on a ceramic plate held over an aluminum sleeve. Four compression springs supported this plate to provide the required degree of movement to establish good thermal contact with the test section and also to accommodate for any expansion during testing. A shaft pin connected the bottom garolite plate and the work desk to ensure stability of the setup. A National Instruments cDaq-9172 data acquisition system with NI-9213 temperature module was used to record the temperatures. A Lab-VIEWVR virtual instrument displayed and calculated the surface temperature and heat flux.

Test Section

The test section employed in this study consisted of a 17 mm × 17 mm copper test surface with a central 10 mm × 10 mm central area exposed to boiling liquid, similar to Jaikumar and Kandlikar [5] (refer Fig. 3 in Ref. [5]). The heater side consisted of a shaft with three thermocouple holes spaced 3-mm apart along the vertical axis to calculate the heat flux and surface temperature. An accurate estimation of the surface temperature was possible by inserting three equally spaced (3 mm) K-type thermocouples (diameter = 0.76 mm) into the holes, thereby eliminating the effect of contact resistance in the calculations.

The heat flux to the test section was calculated using 1D conduction equation

$$q'' = -k_{Cu}\frac{dT}{dx} \qquad (1)$$

The temperature gradient dT/dx was calculated using the three-point backward Taylor's series approximation

$$\frac{dT}{dx} = \frac{3T_1 - 4T_2 + T_3}{2\Delta x} \qquad (2)$$

where T_1, T_2, T_3 are the temperatures corresponding to the top, middle and bottom of the test chip under study.

The boiling surface temperature was obtained by using Eq. (1) and is given by

$$T_{wall} = T_1 - q''\left(\frac{x_1}{k_{Cu}}\right) \qquad (3)$$

where T_{wall} is the boiling surface temperature and x_1 is the distance between the boiling surface and thermocouple T_1; x_1 was equal to 1.5 mm for all the test surfaces.

Uncertainty Analysis

An uncertainty analysis similar to Jaikumar and Kandlikar [5] were conducted on the test samples. Cumulatively, the bias and precision errors that arise due to calibration and precision errors were accounted for in the calculations. The parameters contributing to the errors are the thermocouple calibrations, thermal conductivity of copper, and the distance between thermocouple spacing on the test chip. The method of partial sums was used to estimate the errors in heat flux, HTC, and wall superheat temperature. The maximum uncertainty in wall superheat was ±0.4 °C at a wall superheat of 20 °C. The errors in heat flux and HTC are shown as error bars in the respective plots. The maximum uncertainty in heat flux at CHF was less than 6% for all the test surfaces investigated here.

Surface Preparation

The heat transfer surfaces were prepared by combining copper and GO coatings using two coating techniques: (i) screen printing and (ii) electrodeposition. Sintered [3,15] and electrodeposited [30] porous copper particles are shown to increase the nucleation
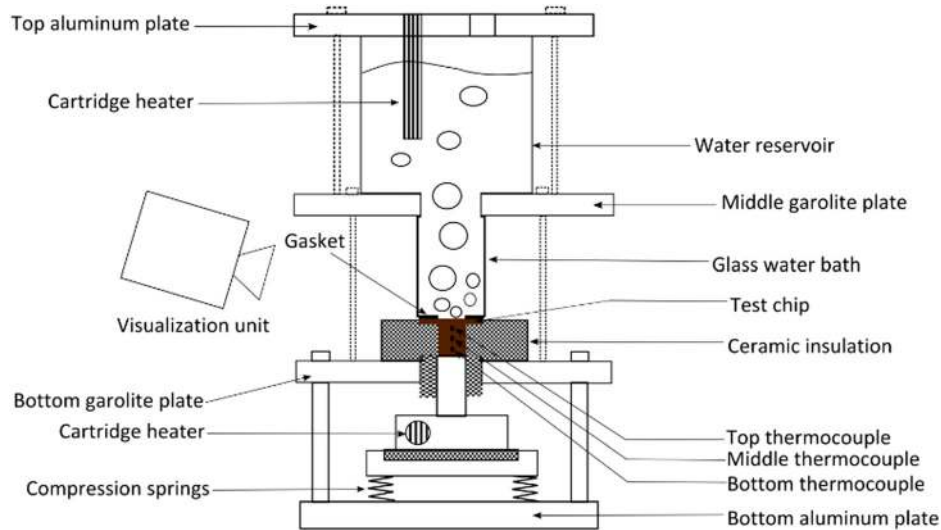
Fig. 3 Pool boiling experimental setup [5]

site density and wickability by enhancing thin film evaporation. A combination of microscale surface morphologies using copper and graphene coatings are generated here and their pool boiling performance with distilled water at atmospheric pressure is investigated. The details of the coating techniques are described next.

Screen Printing. Screen printing is a widely used technique employed in the industry to create a uniform coatings between 5 and 50 μm. In this study, the GO solution was mixed with copper particles to create a paste. The GO solution was prepared using a simple electrochemical technique using an oxygen embrittlement liquid exfoliation technique [31]. The average hydrodynamic diameter of the GO sheets was found to be 1000 nm using dynamic light scattering (DLS) instrument. Hydrodynamic diameter was measured by placing 1 mL of sample in a quartz cuvette (10 × 10 × 45 mm) with 120 s equilibration time. The average hydrodynamic diameters were based on 11 scans and three measurement cycles. The chemical stability of the coatings was confirmed using energy dispersive spectroscopy (EDS) data. The presence of carbide, which is indicative of any reactions with the copper substrate, was not observed in the samples.

The GO was combined with the copper particles (mean particle size = 15 μm) commercially obtained from 3M. Four test chips

(SP-1–SP-4) were generated by varying the amount of GO in the coatings while keeping the amount of copper constant in all the surfaces. A paste was created by adding a commercially available screen printing binder (Nazdar 9627) and subsequently mixing it using a micromixer (Thinky® micromixer) to ensure uniform distribution of GO in the copper paste. The amount of binder added was constant in all the cases. The coating thickness was measured using a confocal laser scanning microscope at the edge location of the test chip separating the coated and noncoated regions. To exercise close control over the coating thickness, a single-pass screen printing process was used similar to Jaikumar and Kandlikar [14]. The coating thickness was ∼35 ± 3 μm for all the surfaces. Substrate bonding was achieved using a sintering process similar to that reported by Jaikumar and Kandlikar [5]. The sintering temperature was 800 °C for a duration of 2 h in an inert helium atmosphere. An intermediate step in the sintering process was introduced to eliminate the binder from the coatings. This was achieved by holding the single-zone furnace temperature at 450 °C for a duration of 1 h. The Fourier transform infrared spectroscopy (FTIR) results presented in Fig. 4 confirm the elimination of other materials from the coatings and are described in detail later. The advancing, receding contact angles and contact angle hysteresis for these surfaces are shown in Table 1.
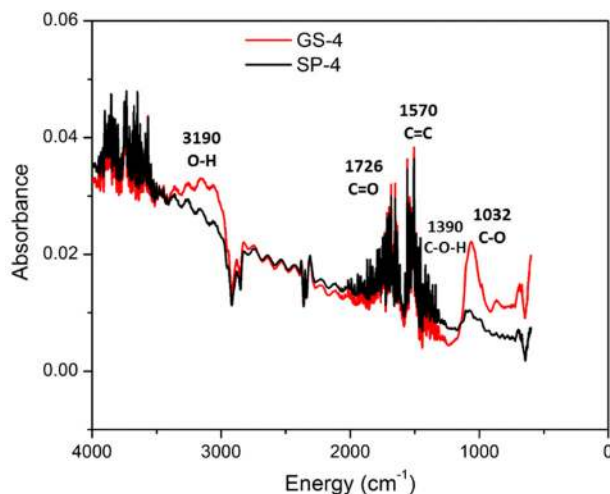
Electrodeposition. Electrodeposition is a simple technique which involves ion reduction at cathode by passing direct current through the solution. Patil and Kandlikar [30,32] used a two-step electrodeposition technique to coat porous copper particles on a copper substrate. A similar arrangement was used in this study. Copper and graphite electrodes formed the cathode and anode, respectively. The electrolyte consisted of 0.8 M copper sulfate solution and 1.5 M sulfuric acid. GO solution was subsequently added to the bath. Two electrochemical methods were

Fig. 4 FTIR spectrum for the screen-printing and electrodeposition samples

Table 1 Test matrix developed with a screen-printing technique

Test chip	% GO (by mass)	Contact angles		
		Receding	Advancing	Hysteresis
Plain chip	—	43	100	57
SP-1	0.2	13.5	69.8	56.3
SP-2	0.4	10.6	81.8	71.2
SP-3	0.6	18.3	117.8	99.5
SP-4	1.0	18.4	118.5	100.1

employed (a) galvanostatic—constant current density and (b) chronoamperometry—constant potential. Protich et al. [33] have shown the addition of GO in a chronoamperometry process results in unique morphologies. The evolution of hydrogen bubbles during the process is shown to create dense porous matrices. The hydrogen bubbles serve as template structures. In the galvanostatic process, the volumetric composition of GO was varied between 1% and 2.5% in the bath to generate the test surfaces (GS-1–GS-4). A two-step deposition process involving deposition for 15 s and substrate bonding for 2400 s was employed. This results in a coating thickness of $\sim 45 \pm 4$ μm for the samples generated using this technique. For the chronoamperometric process, the deposition time was varied between 500 and 1500 s, which resulted in a coating thickness of 40 ± 6 μm. A summary of the test surfaces and their respective contact angles and hysteresis is shown in Table 2.

Chemical Characterization of Heat Transfer Surfaces

FTIR. A Fourier transform infrared (FTIR) spectroscopy (Shimadzu IR Prestige 21) was used to confirm the presence of GO on the substrate. Figure 4 shows the absorption peaks arising from the molecular vibrations of functional groups associated with the coatings. The plot represents the light absorbance by the molecules as a function of wavelength. The characteristic peaks of C=O including stretching vibration of carboxyl group at 1726 cm^{-1}, O–H deformation vibration resulting from C–OH at 1390 cm^{-1}, and C–O stretching vibration at 1032 cm^{-1} was observed here. The peak at 1570 cm^{-1} corresponding to the presence of aromatic rings (C=C) is also seen. The broad peak between 3400 and 3100 cm^{-1} is attributed to O–H stretching from water vapor. The C = C, C = O, C–OH peaks confirm the presence of GO on the surface. Furthermore, typical C–H bonds that arise from organic binders (in the case of screen-printing samples) were absent in the spectrum.

Contact Angles. The effect of contact angle on the pool boiling CHF was modeled by Kandlikar [34] in his force-based CHF equation. Numerous graphene-based studies [24,35] have also highlighted that the wettability played a significant role in the performance. Therefore, the advancing and receding contact angles were measured on the developed surfaces. Raj et al. [26] have shown that the advancing contact angles are a true representation of the surface wettability on graphene structures. The receding contact angles are dominated by variations caused due to surface defects. In this study, the porosity created by the coatings is expected to amplify the effects due to defects. Therefore, the advancing contact angle and contact angle hysteresis, defined as the difference between the advancing and receding contact angles, are used to compare the surface wettability effects.

Comparison of Advancing Contact Angles. In the screen-printed (SP-1–SP-4) copper–graphene surfaces, the advancing contact angles lie between 60 deg and 120 deg. Also, an increasing trend in the advancing contact angles with GO composition is seen (see Table 1). The advancing contact angles in the
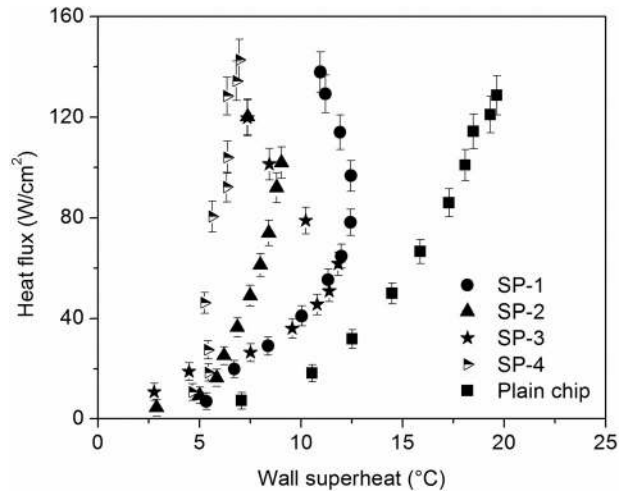

Fig. 5 Pool boiling results for SP-1–SP-4 with distilled water at atmospheric pressure

chronoamperometry cases were between 87 deg and 126 deg. In the case of galvanostatic electrodeposited samples, the advancing contact angles are lower than 60 deg. In this data set, the contact angle decreases with increase in graphene composition. The microscale morphology is postulated to have a significant bearing on the contact angles as seen by the relatively low contact angles with the galvanostatic samples which is discussed in detail later.

Results and Discussion

Pool boiling performance of all the test surfaces shown in Tables 1 and 2 were investigated. The primary objective of this study was to study the effect of combining porous coatings and graphene in a systematic manner. To serve as a baseline, a plain copper chip was also tested. It resulted in a CHF, and HTC at CHF, of 128 W/cm^2 and 65 kW/m^2°C, respectively. Additionally, a plain copper surface coated with porous copper (without GO) under similar conditions was also experimentally tested. This resulted in a CHF of 140 W/cm^2, 140 W/cm^2, and 122 W/cm^2 for screen-printed, chronoamperometry, and galvanostatic coating techniques. The corresponding wall superheats at CHF were 9 °C, 11 °C, and 18 °C, respectively.

Pool Boiling Tests on Screen-Printed Surfaces: Type-I Enhancement. Figure 5 shows the pool boiling curves for the chips prepared using screen-printing. The coatings consisted of sintered-copper and GO. The amount of GO was varied from 0.2% to 1%. The CHF, defined as the upper nucleate boiling limit, was similar to that of a plain chip for all the tests surfaces investigated here. A drastic reduction in the wall superheat is observed

Table 2 Test matrix and surface details developed using electrodeposition techniques (chronoamperometry and galvanostatic)

Electrochemical method	Test chip	% GO (by volume)	Deposition time (s)	Contact angles		
				Receding	Advancing	Hysteresis
	Plain chip	—	—	43	100	57
Galvanostatic (GS)	GS-1	0.5	Step-1: 15	22.4	58.1	35.6
	GS-2	1		14.3	36.4	22.1
	GS-3	1.5	Step-2: 2400	13	33.6	20.6
	GS-4	2.5		13.5	42.6	29.1
Chronoamperometry (CA)	CA-1	2.5	500	48.5	125.6	77.1
	CA-2		1000	35	95.4	60.4
	CA-3		1200	32.4	87	54.6

for all the surfaces investigated. The wall superheats reported for the test chips were less than 10 °C.

Figure 6 shows the variation of HTC with heat flux for the screen-printed surfaces reported in Fig. 5. The heat dissipation capability of a surface can be understood from this plot. The trend indicated that the HTC increases with increase in heat flux. At CHF, a maximum HTC of 194 kW/m^2 °C was obtained with the SP-4-coated surface. This HTC translates to an enhancement of ~200% increase in HTC when compared to a plain chip. Chip SP-1, SP-2, and SP-3 had HTC's of 126 kW/m^2 °C, 163 kW/m^2 °C, and 164 kW/m^2 °C, respectively.

CHF Enhancement: Effect of Wicking. Wickability of a surface is shown to be responsible for the enhancement in CHF [8]. The wicking rates of each surface were measured by visualizing the dynamic spreading behavior of a drop placed on these surfaces. The volumetric change in a liquid droplet of a fixed volume was captured for a duration of ~75 s using a VCA Optima goniometer. Figure 7 summarizes the wicking rates obtained with the screen-printed copper-GO (SP-1–SP-4) test surfaces. In this data set (SP-1–SP-4), the coatings exhibit poor wickability as seen by the low volume of liquid wicked into the coatings. A sintered-copper porous coating without GO results in a wicking rate of 0.99 mm/s, which is significantly higher than that observed on SP-1–SP-4. This correlates well with the CHFs obtained from these samples, which are similar to that of a plain chip (~128 W/cm^2). Although previous studies have indicated high wickability with sintered-copper coatings [3], the addition of GO seems to significantly alter this behavior as demonstrated here. Since the CHF is similar to a plain chip, the contact angle change for SP-1–SP-4 cannot explain the reduction in wall superheats. Therefore, we identify alternate mechanism to influence the enhancement in these surfaces.

Reduction in Wall Superheats: Effect of Additional Nucleation Sites. The irregular porous matrix of the coatings results in a range of cavity sizes on these coatings. The model proposed by Hsu [36] determines the cavity sizes that nucleate at different wall superheats

$$D_{\max}, \ D_{\min} = \frac{\delta_t C_2}{C_1} \frac{\Delta T_w}{\Delta T_w + \Delta T_{\text{sub}}}$$
$$\times \left[1 \pm \sqrt{1 - \frac{8 C_1 \sigma T_{\text{sat}} (\Delta T_w + \Delta T_{\text{sub}})}{\rho_v h_{fg} \delta_t (T_w)^2}} \right] \quad (4)$$

where $C_1 = 1 + \cos\theta$ and $C_2 = \sin\theta$. The application of Hsu's model [36] to the results will be able to estimate the cavity sizes
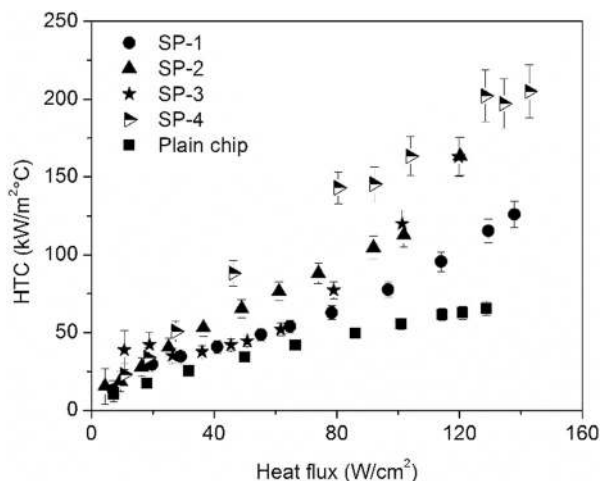
that nucleate at the point where the curve begins to shift to the left at higher heat fluxes. Figures 8(a) and 8(b) show the minimum and maximum cavity diameters for the contact angles corresponding to each surface for the range of wall superheats observed here. The plot shows the potential nucleation cavity diameters for the surfaces: 25–1.9 μm for SP-1, 19–1.4 μm for SP-2, 33–2.4 μm for SP-3, and 34–2.8 μm for SP-4 estimated using Eq. (4). A HTC of 6000 W/m^2 °C was used assuming linear thermal boundary layer while calculating the boundary layer thickness in each sample similar to Ref. [37]. Kruse et al. [37] showed that temperature gradient induced by microstructure height also plays a critical role in the range of cavity sizes that become available for nucleation. Furthermore, they stated that low thermal conductivity materials introduce large thermal gradients which are beneficial in reducing wall superheats at higher heat fluxes.

The scanning laser confocal images shown in Fig. 9 illustrate the range of cavity sizes available for nucleation on the SP-1–SP-4 surfaces. The images were obtained using a Keyence laser confocal microscope using a 10× magnification lens with an approximate working distance of 25 mm. The cavity sizes are within the predicted nucleating range corresponding to each test surface. At the point where the curve begins to shift to the left, the effects arising from additional cavities is amplified. Consequently, the HTC increases significantly due to the increased contribution from the rapid nucleation activity.

The effect of deposition through screen-printing results in a typical sintered-morphology with a range of cavity sizes 1–30 μm. While the addition of graphene has shown to alter the contact angles in these copper-GO porous coatings, the effect of wicking is also significantly diminished inside the features. It is postulated here that the GO encapsulates the porous copper, thereby inhibiting liquid to be wicked into the coatings. Figures 10(a) and 10(b) show the morphological features on the SP-4 surface examined on a JSM-6400V scanning electron microscope (SEM), JEOL, Ltd., Tokyo, Japan, at an accelerating voltage of 15 kV. A typical sintered-morphology similar to Jaikumar and Kandlikar [5] was observed on these surfaces. Figures 10(c) shows the SEM image obtained at 5000× on which the elemental analysis was conducted. Figure 10(d) shows the elemental analysis which confirms the presence of carbon, oxygen, and copper in the coatings.

The enhancement mechanism in these structures is primarily due to increased nucleation activity. The range of cavity sizes available for nucleation both in the planar and along the coating thickness is identified as the main contributing mechanism for the increase in HTC. This causes the boiling curve to shift to the left owing to the rapid nucleation activity. On the other hand, the wicking rates in these coatings are small indicating that liquid retention in the wick structure did not contribute to the
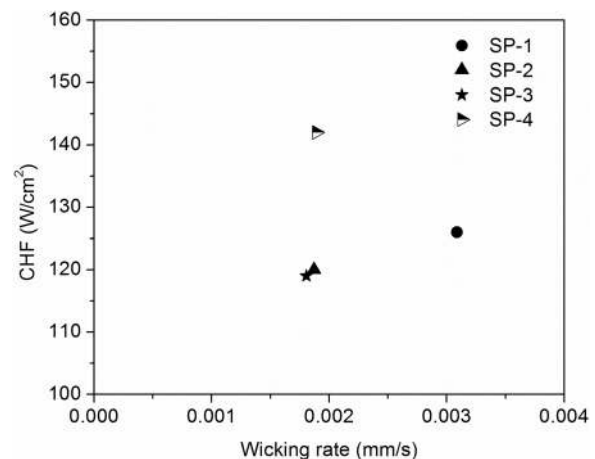

Fig. 6 Heat transfer performance curves for the screen-printed samples (SP-1–SP-4)

Fig. 7 Wicking rates obtained with the screen-printed samples. These surface exhibit poor wickability.

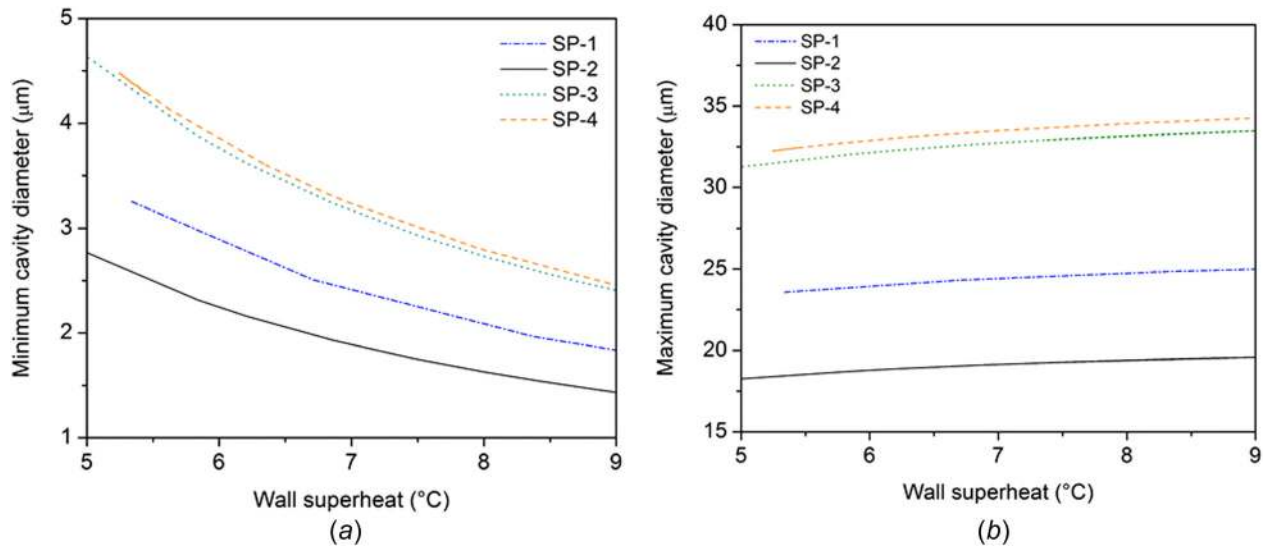**Fig. 8** (*a*) Maximum cavity diameter and (*b*) minimum cavity diameter for the samples as a function of wall superheat using Hsu's model [36]. At higher wall superheats, smaller cavities begin to nucleate which forms the basis of enhancement on these surfaces.

enhancement. This is evident from the low CHF values observed for these samples.

Chronoamperometry Electrodeposition Process: Type-II Enhancement. Figure 11 shows the pool boiling results obtained with GO-copper samples CA-1, CA-2, and CA-3 prepared using the chronoamperometry electrodeposition process (see Table 2). In this data set, the deposition time was varied between 500 and 1500 s to create three test surfaces. A maximum CHF of 216 W/cm^2 was achieved with the surface corresponding to the shortest coating duration (500 s). The CA-2 and CA-3 surfaces reached a CHF of

176 W/cm^2 and 188 W/cm^2, respectively. The wall superheats in these surfaces were similar to that on a plain copper chip. The HTC at CHF for the samples CA-1, CA-2, and CA-3 were 86 kW/m^2 °C, 60 kW/m^2 °C, and 78 kW/m^2 °C, respectively.

CHF Enhancement: Effect of Contact Angles. The surfaces prepared under this category show a well-strung morphology unlike the sintered-morphology seen with SP-1–SP-4. Therefore, the authors postulate that the CHF enhancement is dependent on the dynamic contact angles which dictate the wettability on the surface. The surfaces here exhibit high CHFs which is attributed to the change in the advancing contact angles influenced by the
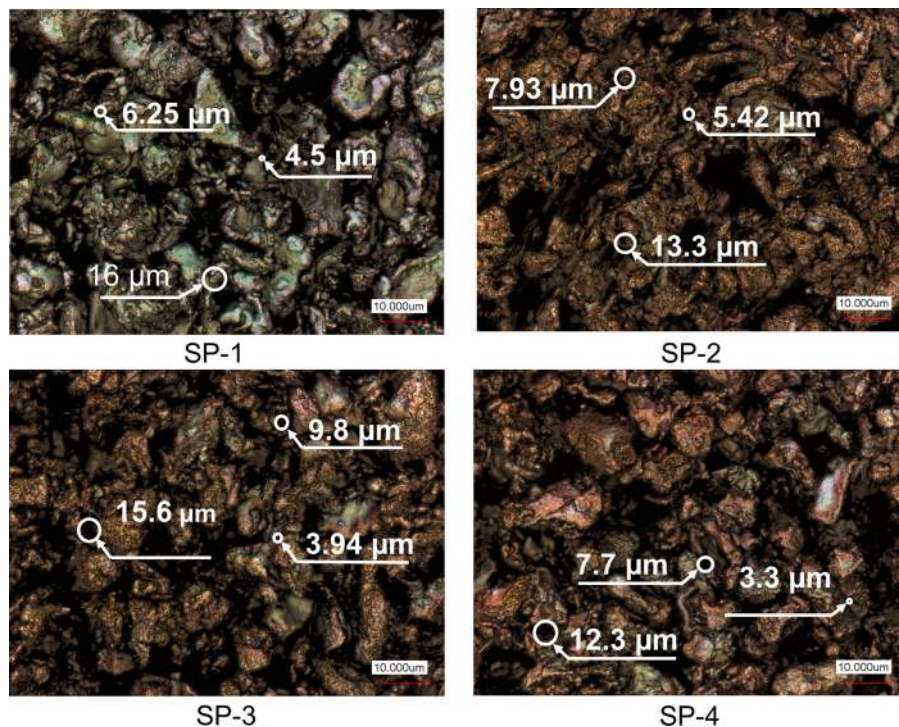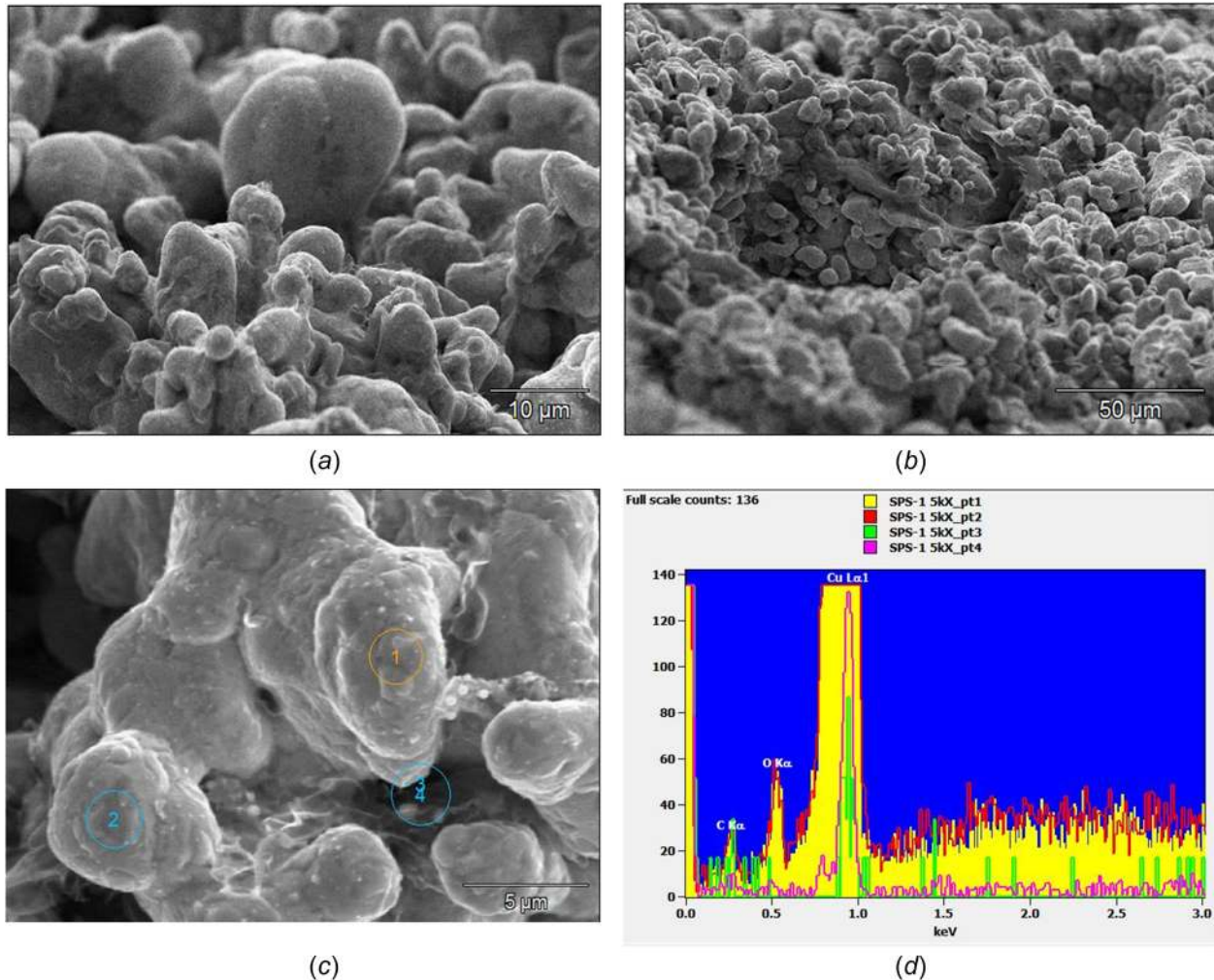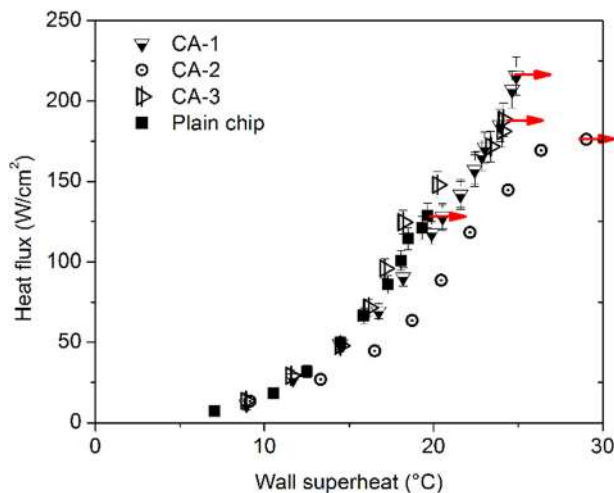

Fig. 9 Confocal laser scanning images showing range of cavities available for nucleation in the samples. These cavities fall within the range established using Hsu's criterion and nucleate when superheat conditions are met.

(a)

(b)

(c)

(d)

Fig. 10 SEM images of the coated samples at (a) 2 k×, 66 deg tilt, (b) 600×, (c) 5 k× magnification, and (d) elemental analysis. These images confirm the deposition of copper and carbon as seen by the intensity signals in (d).

roughness on the surface. Hierarchical microstructures are shown to manipulate the surface forces holding the contact line due to its large effective contact line length on these surfaces [38]. The arithmetic mean roughness, R_a, values for CA-1, CA-2, and CA-3 were 13.7 μm, 8.93 μm, and 12.33 μm, respectively. The

corresponding CHF values were 216 W/cm^2, 176 W/cm^2, and 188 W/cm^2, respectively. The plain chip had a R_a and CHF values of 1.1 μm and 128 W/cm^2, respectively.

Type II: Heat Transfer Enhancement Mechanism. The surfaces (CA-1, CA-2, and CA-3) tested here exhibit an increase in CHF without a reduction in wall superheat. These surfaces benefit from large advancing contact angles which significantly increase the CHF. Figure 12 shows the SEM images obtained on the surface. The image indicates that the deposition resulted in a hierarchical matrix of copper decorated with graphene. In such an arrangement, the roughness-augmented wettability is amplified as the contact angles are significantly influenced by the hierarchical structures similar to that reported by Chu et al. [38]. Therefore, it can be concluded that type-II structures benefit from roughness-augmented wettability, but the absence of rapid nucleation activity at high heat fluxes due to the morphology-induced effects causes the wall superheats to increase. Further examination of the test surfaces and additional experiments are warranted to confirm the mechanism in this category.

Galvanostatic Electrodeposition Process: Type-III Enhancement. Figure 13(*a*) shows the pool boiling curves obtained with the GS-1–GS-4. The GO composition in these samples was varied between 0.5% and 2.5% by volume. The deposition was carried out in a carefully designed electrochemical cell using a galvanostatic method as discussed previously. GS-1, GS-2, and GS-3
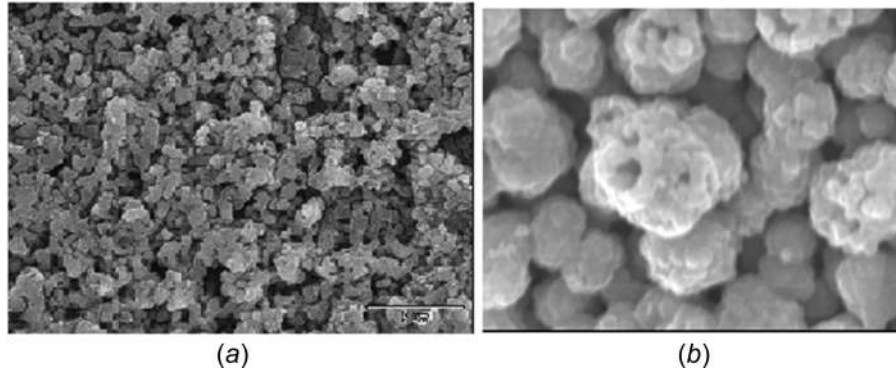

Fig. 11 Pool boiling results obtained with CA-1–CA-3 with distilled water at atmospheric pressure

Fig. 12 SEM images depicting well-strung features on CA-1

reached a CHF of 135 W/cm^2, 169 W/cm^2, and 194 W/cm^2, respectively. A CHF of 220 W/cm^2 was obtained with GS-4 corresponding to the sample with the maximum GO composition of 2.5%. To the best of the authors' knowledge, this is currently the highest reported CHF with GO-based coatings. Contrary to the results reported with screen-printed samples (SP-1–SP-4), the test surfaces in this data set resulted in an increase in CHF with a simultaneous reduction in wall superheat at higher heat fluxes.

Figure 13(*b*) shows the HTC plots obtained for the surfaces prepared using the galvanostatic process. In these samples, a significant increase in HTC in addition to CHF increase was observed. A maximum HTC of 72 kW/m^2 °C, 155 kW/m^2 °C, 103 kW/m^2 °C, and 155 kW/m^2 °C at CHF was achieved with GS-1, GS-2, GS-3, and GS-4, respectively. The trend in the investigated surfaces suggests that the CHF increased with an increase in the GO concentration.

CHF Enhancement: Wickability of the Surface. The wicking rates play a significant role in enhancing the CHF. Rahman et al. [8] demonstrated this effect by introducing a dimensionless parameter, wicking number (Wi), which directly correlated to the increase in CHF using bio-templated structures. The enhancement in CHF is attributed to the increase in liquid retention in the wick structure which promotes evaporation. Figure 14 shows the variation of CHF with (1 + Wi) for the surfaces investigated here. It must be noted that the wicking rate in the two studies were computed using different methods. The wicking number is calculated using Eq. (5) as described by Rahman et al. [8]

$$\mathrm{Wi} = \frac{V_o'' \rho_l}{\rho_v^{\frac{1}{2}}[\sigma g (\rho_l - \rho_v)]^{\frac{1}{4}}} \qquad (5)$$

Fig. 14 CHF trend as a function of wicking number (Wi). High Wi represents a surface with high wickability contributing to increase in CHF.

where V_o'' is the wicking rate (m/s), ρ_l and ρ_v are the liquid and vapor densities (kg/m^3), g is the acceleration due to gravity (m/s^2), and σ is the surface tension force (N/m). The wicked volume (mm^3/s) is estimated as the droplet volume change over time using a VCA Optima goniometer. The wicking rate (mm/s) is calculated by normalizing the wicked volume over the droplet impingement area. This method offers a simple technique to characterize wickability on moderate and low wicking structures.
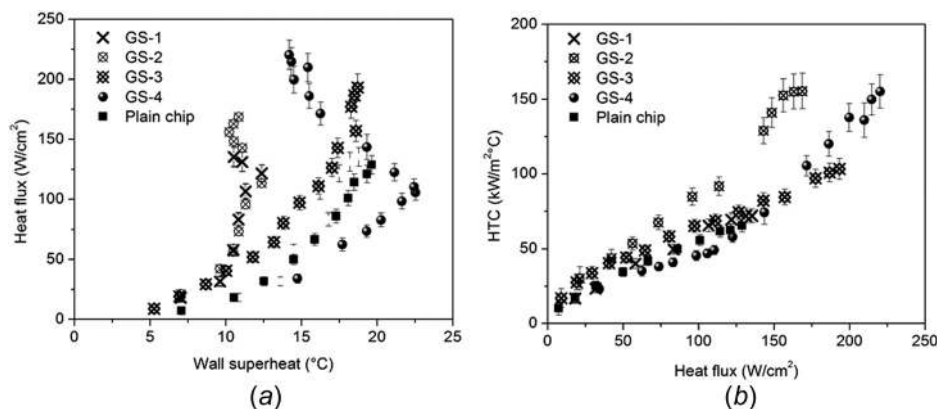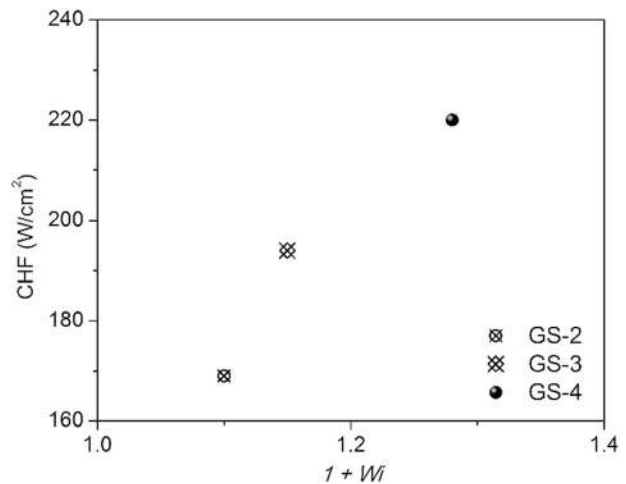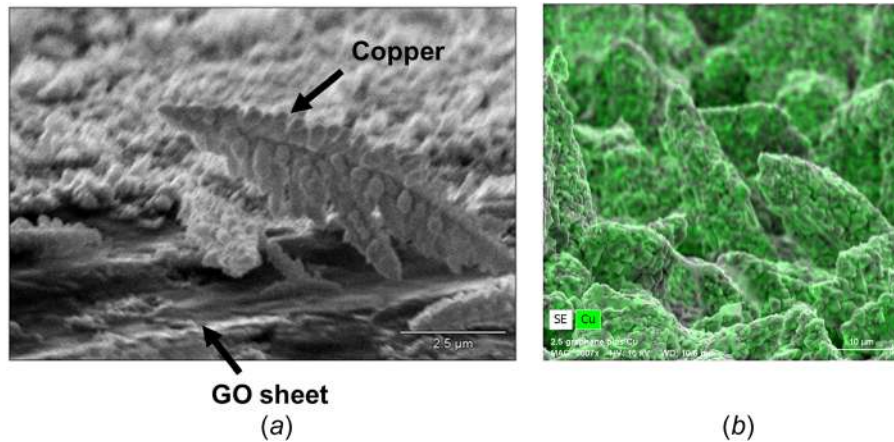

Fig. 13 (*a*) Pool boiling results obtained with distilled water at atmospheric pressure with GS-1–GS-4 and (*b*) Heat transfer performance curves

Fig. 15 SEM images of the electrodeposited surface using galvanostatic method: (*a*) dendritic copper structures with underlying GO sheets at 10 k×, 70 deg tilt and (*b*) energy dispersive X-ray spectroscopy (EDS) showing copper mapping confirming dendritic structures were made of copper

It is noted from Fig. 14 that the CHF increases with an increase in the wicking number. The application of the CHF correlation proposed by Rahman et al. [8] predicts a CHF of less than 150 W/cm^2, which is less than the experimental values obtained in this data set. Therefore, we recognize that additional mechanisms were further responsible for the enhancement.

Additional Nucleation Sites and Microlayer Partitioning Mechanisms. In the samples investigated here (GS-1–GS-4), the HTC is significantly increased due to the low wall superheats at relatively higher heat fluxes. This behavior is similar to that observed with the screen-printed samples (SP-1–SP-4) but with a substantial increase in CHF. GS-1 exhibits similar effect to the screen-printed samples where the CHF is similar to that observed on a plain chip. Therefore, this surface can be categorized under type-I enhancement. Similarly, GS-3 can be classified under type-II enhancement. GS-2 and GS-4, in addition to wicking, have increased nucleation sites that are activated under suitable superheat conditions and contribute toward decreasing the wall superheat. The mechanism for such a trend is attributed to the range of cavity sizes available for nucleation as discussed previously. The nucleation activity is further promoted by the enhanced evaporation through microlayer partitioning mechanisms. Maroo's group introduced this mechanism by fabricating silicon ridges in the nano/microscale [11,29]. The microlayer is a thin liquid film that forms underneath a growing bubble. By employing ridges, Zou and Maroo [11,29] demonstrated that the microlayer gets partitioned which results in additional liquid volume available for evaporation. Through analytical models, they demonstrated that this behavior results in increased bubble volume and frequencies. Similarly, Jaikumar et al. [27] have shown the microlayer partitioning on graphene surfaces contributed toward increasing the growth rates and bubble frequency.

Type-III: Heat Transfer Enhancement Mechanism. The enhancements in CHF and HTC are due to the relative effects of wicking and additional nucleation sites. The microscale morphology of the samples plays a critical role in enhancing wicking and promoting nucleation. Figure 15 shows the SEM images of the test surface (GS-4). The unique morphology obtained with these samples shows the clear separation of copper and GO sheets deposited through the process. The copper appears as dendritic structures as confirmed by the SEM images obtained (see Fig. 15(*b*)), which is similar to that reported by Patil et al. [30]. GO seems to get deposited as sheets underlying the dendritic copper features. An extensive characterization study is being conducted in the authors' lab as future work for such features. These features seem to promote wicking through the copper-dendrites and nucleation through the

underlying GO sheets. The nucleation activity increases due to microlayer partitioning mechanisms, as demonstrated by Jaikumar et al. [27] and Zou and Maroo [11]. This arrangement results in an increase in both CHF and HTC under type-III characteristics demonstrated here.

The effect of wicking and increased nucleation activity seems to be the main contributing mechanisms in type-III enhancement. This is attributed to the competing nature of the two mechanisms induced by the coatings. Further studies are warranted to explain the relative merits of the two mechanisms in a unified model.

Conclusions

A detailed experimental study was conducted using screen-printing and electrodeposition techniques to demonstrate the three boiling characteristics. A combination of copper and GO was used to develop the corresponding heat transfer surfaces. FTIR, SEM, and confocal laser scanning images were obtained to further understand the microscale morphologies. The pool boiling results were obtained with distilled water at atmospheric pressure. The following conclusions were drawn from this study:

(1) Three boiling characteristics, type I, type II, and type III, have been identified based on the enhancement observed in CHF, HTC, or both, respectively. These characteristics are closely linked with the surface morphology of the GO coated surfaces and heat transfer mechanisms.

(2) Type-I boiling characteristic results in a significant reduction in the wall superheat without an increase in CHF when compared to a plain surface. Four surfaces (SP-1–SP-4) were generated using a screen-printing technique. The GO composition in the surfaces was varied between 0.2% and 1% by mass of the copper composition in the matrix. The lowest wall superheat of 7 °C was observed with SP-2 and SP-3 test surfaces. A typical sintered-morphology was observed using SEM images. The rapid nucleation activity contributed to the enhancement in type-I boiling enhancement as a consequence of the available nucleation sites.

(3) A chronoamperometry electrodeposition technique was used generate three surfaces (CA-1–CA-3) to demonstrate type-II boiling characteristics. In this category, a significant increase in CHF without a reduction in the wall superheat was observed. The deposition duration was varied between 500 and 1500 s to create unique morphologies. The SEM images indicated hierarchical matrix which influenced the liquid wettability through roughness augmentation. These surfaces do not show the curve shifting to the left at higher heat fluxes. A maximum CHF of 216 W/cm^2 which

translated to an enhancement of 69% was obtained with the surface (CA-1) corresponding to the shortest coating duration (500 s) when compared to a plain surface.

(4) In type-III, an increase in CHF is accompanied with a decrease in wall superheats at higher heat fluxes. A galvanostatic technique with GO composition of 0.5–2.5% (by volume) was used to generate four surfaces (GS-1–GS-4) in this data set. The electrodeposition technique seems to create separated depositions of dendritic copper and GO sheet structures. The wicking-enabled dendritic structures enhance the CHF, while the underlying GO sheets promote nucleation characteristics through microlayer partitioning mechanisms. A CHF enhancement of 72% and wall superheat reduction of 43% was obtained with the surface corresponding to the maximum GO concentration.

Acknowledgment

Nomenclature

CHF = critical heat flux (W/m^2)
dT = temperature gradient ($^\circ$C)
g = gravitational acceleration (m/s^2)
GO = graphene oxide
h_{fg} = latent heat of vaporization (J/kg)
HTC = heat transfer coefficient (W/cm^2 $^\circ$C)
k_{Cu} = thermal conductivity of copper (W/m K)
q'' = heat flux (W/m^2)
R_a = arithmetic mean roughness (μm)
T_{wall} = surface temperature of the test section ($^\circ$C)
θ = dynamic receding contact angle (deg)
ρ_g = density of vapor (kg/m^3)
ρ_l = density of liquid (kg/m^3)
σ = surface tension (N/m)

References

[1] Mandrusiak, G. D., and Carey, V. P., 1989, "Convective Boiling in Vertical Channels With Different Offset Strip Fin Geometries," ASME J. Heat Transfer, **111**(1), pp. 156–165.
[2] Pastuszko, R., and Piasecka, M., 2012, "Pool Boiling on Surfaces With Mini-Fins and Micro-Cavities," J. Phys.: Conf. Ser., **395**, p. 012137.
[3] Li, C., and Peterson, G. P., 2007, "Parametric Study of Pool Boiling on Horizontal Highly Conductive Microporous Coated Surfaces," ASME J. Heat Transfer, **129**(11), pp. 1465–1475.
[4] Dong, L., Quan, X., and Cheng, P., 2014, "An Experimental Investigation of Enhanced Pool Boiling Heat Transfer From Surfaces With Micro/Nano-Structures," Int. J. Heat Mass Transfer, **71**, pp. 189–196.
[5] Jaikumar, A., and Kandlikar, S. G., 2015, "Enhanced Pool Boiling Heat Transfer Mechanisms for Selectively Sintered Open Microchannels," Int. J. Heat Mass Transfer, **88**, pp. 652–661.
[6] Jaikumar, A., and Kandlikar, S. G., 2016, "Ultra-High Pool Boiling Performance and Effect of Channel Width With Selectively Coated Open Microchannels," Int. J. Heat Mass Transfer, **95**, pp. 795–805.
[7] Kandlikar, S. G., 2013, "Controlling Bubble Motion Over Heated Surface Through Evaporation Momentum Force to Enhance Pool Boiling Heat Transfer," Appl. Phys. Lett., **102**(5), p. 051611.
[8] Rahman, M. M., Ölçeroğlu, E., and McCarthy, M., 2014, "Role of Wickability on the Critical Heat Flux of Structured Superhydrophilic Surfaces," Langmuir, **30**(37), pp. 11225–11234.
[9] Chu, K.-H., Enright, R., and Wang, E. N., 2012, "Structured Surfaces for Enhanced Pool Boiling Heat Transfer," Appl. Phys. Lett., **100**(24), p. 241603.
[10] Betz, A. R., Xu, J., Qiu, H., and Attinger, D., 2010, "Do Surfaces With Mixed Hydrophilic and Hydrophobic Areas Enhance Pool Boiling?," Appl. Phys. Lett., **97**(14), p. 141909.
[11] Zou, A., and Maroo, S. C., 2013, "Critical Height of Micro/Nano Structures for Pool Boiling Heat Transfer Enhancement," Appl. Phys. Lett., **103**(22), p. 221602.
[12] Kandlikar, S., 2017, "Enhanced Macro-Convection Mechanism With Separate Liquid–Vapor Pathways to Improve Pool Boiling Performance," ASME J. Heat Transfer, **139**(5), p. 051501.
[13] Cooke, D., and Kandlikar, S. G., 2012, "Effect of Open Microchannel Geometry on Pool Boiling Enhancement," Int. J. Heat Mass Transfer, **55**(4), pp. 1004–1013.
[14] Jaikumar, A., and Kandlikar, S. G., 2016, "Pool Boiling Enhancement Through Bubble Induced Convective Liquid Flow in Feeder Microchannels," Appl. Phys. Lett., **108**(4), p. 041604.
[15] Webb, R. L., 1983, "Nucleate Boiling on Porous Coated Surfaces," Heat Transfer Eng., **4**(3–4), pp. 71–82.
[16] O'Hanley, H., Coyle, C., Buongiorno, J., McKrell, T., Hu, L.-W., Rubner, M., and Cohen, R., 2013, "Separate Effects of Surface Roughness, Wettability, and Porosity on the Boiling Critical Heat Flux," Appl. Phys. Lett., **103**(2), p. 024102.
[17] Fan, L.-W., Li, J.-Q., Li, D.-Y., Zhang, L., Yu, Z.-T., and Cen, K.-F., 2015, "The Effect of Concentration on Transient Pool Boiling Heat Transfer of Graphene-Based Aqueous Nanofluids," Int. J. Therm. Sci., **91**, pp. 83–95.
[18] Ahn, H. S., Kim, J. M., Kaviany, M., and Kim, M. H., 2014, "Pool Boiling Experiments in Reduced Graphene Oxide Colloids—Part I: Boiling Characteristics," Int. J. Heat Mass Transfer, **74**, pp. 501–512.
[19] Ahn, H. S., Kim, J. M., Kim, J. M., Park, S. C., Hwang, K., Jo, H. J., Kim, T., Jerng, D. W., Kaviany, M., and Kim, M. H., 2015, "Boiling Characteristics on the Reduced Graphene Oxide Films," Exp. Therm. Fluid Sci., **60**, pp. 361–366.
[20] Ahn, H. S., Kim, J. M., and Kim, M. H., 2013, "Experimental Study of the Effect of a Reduced Graphene Oxide Coating on Critical Heat Flux Enhancement," Int. J. Heat Mass Transfer, **60**, pp. 763–771.
[21] Novoselov, K. S., Fal, V. I., Colombo, L., Gellert, P. R., Schwab, M. G., and Kim, K., 2012, "A Roadmap for Graphene," Nature, **490**(7419), pp. 192–200.
[22] Jaikumar, A., Kandlikar, S. G., and Gupta, A., 2016, "Pool Boiling Enhancement Through Graphene and Graphene Oxide Coatings," Heat Transfer Eng., **38**(14–15), pp. 1274–1284.
[23] Park, S. D., Lee, S. W., Kang, S., Bang, I. C., Kim, J. H., Shin, H. S., Lee, D. W., and Lee, D. W., 2010, "Effects of Nanofluids Containing Graphene/Graphene-Oxide Nanosheets on Critical Heat Flux," Appl. Phys. Lett., **97**(2), p. 023103.
[24] Ahn, H. S., Kim, J. M., Kaviany, M., and Kim, M. H., 2014, "Pool Boiling Experiments in Reduced Graphene Oxide Colloids—Part II: Behavior After the CHF, and Boiling Hysteresis," Int. J. Heat Mass Transfer, **78**, pp. 224–231.
[25] Kim, J. M., Kim, T. J., Kim, J. Y., Kim, M. H., and Ahn, H. S., 2014, "Effect of a Graphene Oxide Coating Layer on Critical Heat Flux Enhancement Under Pool Boiling," Int. J. Heat Mass Transfer, **77**, pp. 919–927.
[26] Raj, R., Maroo, S. C., and Wang, E. N., 2013, "Wettability of Graphene," Nano Lett., **13**(4), pp. 1509–1515.
[27] Jaikumar, A., Gupta, A., Kandlikar, S., Yang, C.-Y., and Su, C.-Y., 2017, "Scale Effects of Graphene and Graphene Oxide Coatings on Pool Boiling Enhancement Mechanisms," Heat Mass Transfer, **109**, pp. 357–366.
[28] Sumith, Y. D., and Maroo, S. C., 2016, "Origin of Surface-Driven Passive Liquid Flows," Langmuir, **32**(34), pp. 8593–8597.
[29] Zou, A., and Singh, D. P., and Maroo, S. C., 2016, "Early-Evaporation of Microlayer for Boiling Heat Transfer Enhancement," Langmuir, **32**(42), pp. 10808–10814.
[30] Patil, C. M., Santhanam, K. S. V., and Kandlikar, S. G., 2014, "Development of a Two-Step Electrodeposition Process for Enhancing Pool Boiling," Int. J. Heat Mass Transfer, **79**, pp. 989–1001.
[31] Santhanam, K. S. V., Kandlikar, S. G., Mejia, V., and Yue, Y., 2016, "Electrochemical Process for Producing Graphene, Graphene Oxide, Metal Composites, and Coated Substrates," Patent No. WO 2016011180 A1.
[32] Patil, C. M., and Kandlikar, S. G., 2014, "Pool Boiling Enhancement Through Microporous Coatings Selectively Electrodeposited on Fin Tops of Open Microchannels," Int. J. Heat Mass Transfer, **79**, pp. 816–828.
[33] Protich, Z., Santhanam, K. S. V., Jaikumar, A., Kandlikar, S. G., and Wong, P., 2016, "Electrochemical Deposition of Copper in Graphene Quantum Dot Bath: Pool Boiling Enhancement," J. Electrochem. Soc., **163**(6), pp. E166–E172.
[34] Kandlikar, S. G., 2001, "A Theoretical Model to Predict Pool Boiling CHF Incorporating Effects of Contact Angle and Orientation," ASME J. Heat Transfer, **123**(6), pp. 1071–1079.
[35] Seo, H., Chu, J. H., Kwon, S.-Y., and Bang, I. C., 2015, "Pool Boiling CHF of Reduced Graphene Oxide, Graphene, and SiC-Coated Surfaces Under Highly Wettable FC-72," Int. J. Heat Mass Transfer, **82**, pp. 490–502.
[36] Hsu, Y. Y., 1961, "On Size Range of Active Nucleation Cavities on Heating Surface," ASME J. Heat Transfer, **84**(3), pp. 207–213.
[37] Kruse, C., Tsubaki, A., Zuhlke, C., Anderson, T., Alexander, D., Gogos, G., and Ndao, S., 2016, "Secondary Pool Boiling Effects," Appl. Phys. Lett., **108**(5), p. 051602.
[38] Chu, K.-H., Joung, Y. S., Enright, R., Buie, C. R., and Wang, E. N., 2013, "Hierarchically Structured Surfaces for Boiling Critical Heat Flux Enhancement," Appl. Phys. Lett., **102**(15), p. 151602.